

DISCOVERY AND MULTI-WAVELENGTH ANALYSIS OF A NEW DISSOCIATIVE GALAXY CLUSTER MERGER: THE CHAMPAGNE CLUSTER

FAIK BOUHRİK,^{1,2} RODRIGO STANCIOLI,² AND DAVID WITTMAN²

¹*California Northstate University
2910 Prospect Park Dr
Rancho Cordova, CA 95670, USA*
²*University of California Davis
One Shields Ave
Davis, CA 95616, USA*

ABSTRACT

We report the discovery of a new binary galaxy cluster merger, the Champagne Cluster (RM J130558.9+263048.4), using a detection method that identifies dynamically active clusters in the redMaPPer SDSS DR8 photometric galaxy cluster catalog. The Champagne Cluster exhibits the classic X-ray morphology of a post-pericenter dissociative galaxy cluster merger: an X-ray peak located between two galaxy overdensities at the same redshift. We conducted a Keck/DEIMOS survey and obtained redshifts for 103 member galaxies. The redshift analysis indicates a relative velocity of 411 ± 180 km/s between the two subclusters, which suggests that the merger is happening near the plane of the sky. We used cosmological simulations to find analogous systems to constrain the time since pericenter (74-250 Myr) and the angle the merger axis makes with the plane of the sky (62° - 90°) at the 68% confidence level. We estimated the bulk temperature (8.20 ± 1.2 keV) and total X-ray luminosity ($7.29 \pm 0.19 \times 10^{44}$ erg \times s^{-1}) of the intracluster medium using *Chandra* archival data.

Keywords: Galaxy cluster (584); Dark matter (353); Galaxy spectroscopy (2171)

1. INTRODUCTION

According to the Λ CDM model of cosmology, density fluctuations in the primordial universe collapsed to form the seeds of cosmic structure. These seeds hierarchically grew to form larger and larger structures through merging and accretion, eventually building galaxy clusters (Frenk & White 2012). In recent decades, galaxy clusters have been established as powerful probes for a host of astrophysical and particle physics processes (Kravtsov & Borgani 2012): the hierarchical formation of large structure in the universe (Cohn & White 2005), rates of star formation in dense environments (Miller & Owen 2003; Mansheim et al. 2017), and the nature and properties of dark matter (Markevitch et al. 2004; Bradač et al. 2008; Dawson et al. 2011; Wittman et al. 2023).

In a major galaxy cluster merger, the three components (dark matter halos, galaxies, and the intracluster medium (ICM)), may become separated (Clowe et al. 2006). Offsets between dark matter, galaxies, and X-ray surface brightness peaks offer rare glimpses into the properties of dark matter, allowing for the constraining

of the scattering cross-section for dark matter particles (Markevitch et al. 2004). It was such an offset exhibited by the iconic Bullet Cluster (1E 0657-56) that provided the first direct evidence for the existence of dark matter and allowed for imposing an upper limit on the self-interaction cross-section for dark matter particles (Clowe et al. 2006; Randall et al. 2008). In the following years, only a handful of such clean bimodal systems were identified, for example A520 (Mahdavi et al. 2007), MACS J0025.4-1222 (Bradač et al. 2008), A1758 (Okabe & Umetsu 2008), and DLSC J0916+2953 (Dawson et al. 2011).

We have been working on a method based on galaxy cluster bimodality, which has allowed for a more targeted search than serendipitous disturbed X-ray morphology detection. We build on the the redMaPPer algorithm (Rykoff et al. 2014; Rykoff et al. 2016), which is a photometric red-sequence galaxy cluster finder designed specifically for large photometric surveys, such as the Sloan Digital Sky Survey (SDSS) DR8 (Aihara et al. 2011). redMaPPer identified 26,111 galaxy cluster candidates in the SDSS DR8 catalog. We select clus-

ters that are not dominated by a single brightest cluster galaxy (BCG), and where the minimum angular separation between the top two BCG candidates is at least $\sim 1'$. Clusters that satisfy these two criteria become candidates for X-ray *Chandra* and XMM-*Newton* archival searches. The location of the X-ray peak between the top two BCG candidates made some merger candidates of particular interest for immediate study, as a dissociative X-ray morphology is indicative of a post pericenter merger that has an axis component in the plane of the sky. Such systems can play a pivotal role in constraining dark matter properties. RM J130558.9+263048.4, the subject of this paper, is one of these candidates. Two other candidates that were discovered using the same method are Abell 56 (Wittman et al. 2023) and RM J150822.0+575515.2 (Stancioli et al. 2024).

In this paper, we assume a Λ CDM cosmology with a $H_o = 69.6$ km/s and $\Omega_o = 0.286$.

2. THE CHAMPAGNE CLUSTER: INITIAL OVERVIEW

For easy reference, we assign the nickname the Champagne Cluster to RM J130558.9+263048.4. redMaPPer includes in its richness calculation the total number of probable cluster members, which leads to a richness of 70 for the Champagne Cluster (Rykoff et al. 2016). The Champagne Cluster is poorer than most binary clusters known to the literature, however it is still richer than 93.7% of the members of the redMaPPer catalog. We estimate its mass (M_{200}) to be $4.65^{+11.50}_{-4.69} \times 10^{14} h^{-1} M_{\odot}$ using the mass-richness relation for the redMaPPer catalog, where the mass was calibrated via SDSS weak lensing data (Simet et al. 2016). SDSS DR8 assigns the spectroscopic redshifts of 0.30812 and 0.30815 to the top two BCG candidates, as indicated in Table 1. Using the relative velocities of the two BCGs as proxies for the relative velocities of the subclusters yields a velocity of one cluster in the frame of the other, Δv_{los} , of only 6 ± 20 km/s. This very low line-of-sight velocity hints at a merger that is happening nearly in the plane of the sky and/or a merger that is at turnaround. In §6 we refine this estimate by using the average redshift for each subcluster as a proxy for the subcluster redshift, and hence velocity.

The angular separation between the BCGs of the two subclusters is $1.17'$, which translates to a physical separation of 335 kpc at the cluster’s redshift.

In Figure 1, we show an X-ray surface brightness contour map overlaid on a DESI Legacy Survey DR10 color image. The location of the X-ray peak along the axis that connects the top two BCG candidates is a good indicator of a post pericenter galaxy cluster merger.

Table 1. Top two BCG candidates for the Champagne Cluster

BCG	R.A.	Decl.	z
Top BCG candidate	196.4954	28.150217	0.30812
2nd BCG candidate	196.5167	28.143211	0.30815

The Champagne Cluster (Planck cluster name: PSZ2 G023.17+86.71) is one of the 83 Planck clusters that host extended radio emissions (radio halos) at the locations of the clusters in the LoTSS-DR2 catalog (Botteon, A. et al. 2022). The halo of the Champagne Cluster extends in the West-East direction, and there are no radio relics associated with it.

3. CHANDRA DATA REDUCTION AND ANALYSIS

The Champagne Cluster was observed by *Chandra* on 2012 November 18 (Observation ID: 15097, PI: Casano). The exposure time was 29500 s. We used CIAO version 4.14 (Fruscione et al. 2006) to analyze the data. We removed the point sources in the field using *wavdetect*, a Mexican-hat wavelet source detection tool, before estimating the global temperature (T_X) and luminosity (L_X). We chose *wavdetect* as our subtraction tool because of its ability to separate closely-spaced point sources, a trait that helps in distinguishing closely separated point sources from extended sources. To extract a spectrum, we enclosed the extended emission area by an elliptical aperture with a semi-major axis of $130''$ and a semi-minor axis of $98''$, which translate to physical axes of 0.61 Mpc and 0.46, respectively, at the redshift of the cluster. We chose as the background region a circular region on the same chip (Chip 3) where no emission was evident. We used the *dmextract* functionality of CIAO to estimate source counts and errors. We used the Sherpa package (Freeman et al. 2001) to fit an *apec* component (thermal bremsstrahlung emission) \times *phabs* component (galactic absorption) to the spectrum. To perform the spectral fitting, we fixed the redshift of the cluster at 0.31 and the metallicity at 0.30 solar. This model gave an estimate for T_X equal to 8.2 ± 1.2 keV. We used the Sherpa package to convert the photon counts to a flux estimate ($5.09 \pm 0.25 \times 10^{-12}$ erg \times s $^{-1}$). We used Wright (2006) to convert the redshift to a luminosity distance to obtain a value for L_X of ($7.29 \pm 0.19 \times 10^{44}$ erg \times s $^{-1}$) in the range 0.5-10.0 keV. We show the best fit curve for the X-ray *Chandra* spectrum of the Champagne Cluster in Figure 2.

4. XMM-NEWTON DATA REDUCTIONS AND ANALYSIS

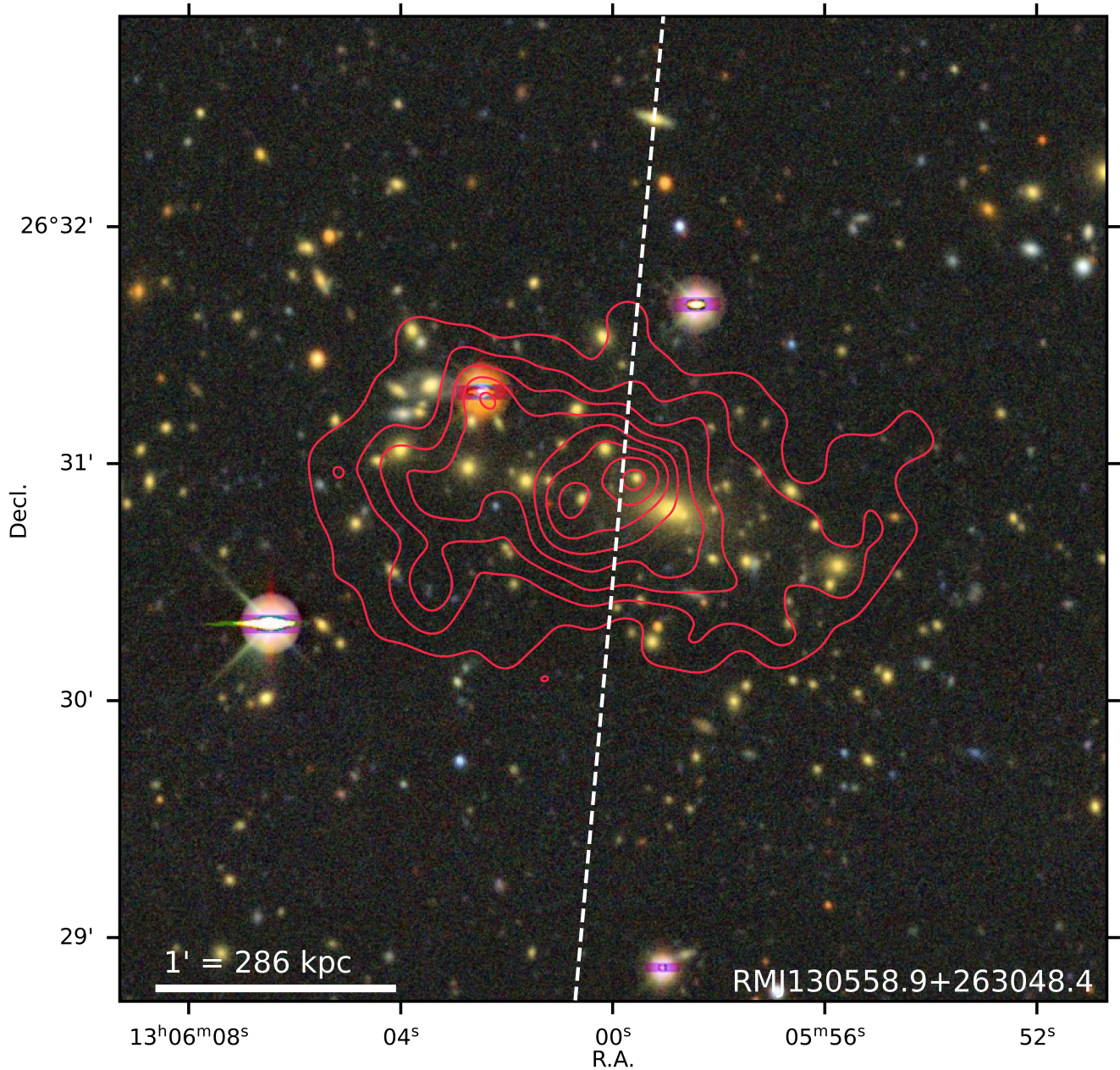


Figure 1. *Chandra* X-ray surface brightness contour map for the Champagne Cluster overlaid on a Legacy Survey color image. The X-ray surface brightness peak is located along the axis that connects the top two BCG candidates. The dashed line separates the two subclusters: Champagne-SE and Champagne-NW. For creating the X-ray image, the energy band 0.5-7.0 keV was selected. Point sources were removed, and the X-ray contours were derived using a Gaussian kernel with a standard deviation of $6.88''$.

The cluster was observed by *XMM-Newton* on 2010-06-05 (ObsID 0650382501, P.I. Allen). The exposure times were 6728, 6741, and 4855 s for the M1, M2, and PN detectors, respectively. We used the *XMM-Newton* Science Analysis System (SAS version 19.0.0.) to extract a global temperature and X-ray luminosity for the cluster. As the *Chandra* observation has a longer exposure

time and better resolution, we use the *XMM-Newton* data as a consistency check on our results from *Chandra*.

We filtered out time intervals contaminated by flare events by imposing a limit of 0.3 (0.6) counts s^{-1} in the 10-12 keV band in the MOS (PN) detectors. Point sources were detected with the SAS task `edetect_chain` and masked out. We chose an identical aperture to the one we used for the analysis of the *Chandra* data, and

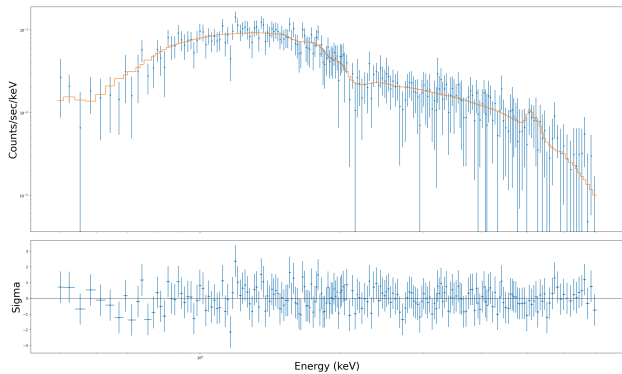


Figure 2. Top panel: The best fit model (apec + phabs) for the *Chandra* X-ray spectrum of the Champagne Cluster. The bulk temperature corresponding to the model is 8.28 ± 1.1 KeV. Bottom panel: Spectrum fitting residuals.

we selected single-to-quadruple events from MOS and single-to-double events from the PN. We subtracted the cosmic and non-cosmic X-ray backgrounds using the double subtraction method described in [Arnaud, M. et al. \(2002\)](#) and blank-sky event lists from stacked, source-removed EPIC observations ([Carter, J. A. & Read, A. M. 2007](#)) available in the XMM-*Newton* blank sky file repository¹. We defined a background region as a circular aperture, with a $70''$ radius, to the SE of the cluster. All event lists were corrected for vignetting using the `evigweight` task.

After obtaining spectra for the three EPIC detectors, we performed a simultaneous fit using XSPEC ([Arnaud 1996](#)). We used an `apec` model for the ICM emission and a `phabs` model for the galactic absorption. We fixed the redshift at 0.308 and the HI column density at $1.08 \times 10^{20} \text{ cm}^{-2}$. Our results indicate an unabsorbed luminosity in the 0.5–10.0 keV energy range of $L_X = 6.65_{-0.34}^{+0.35} \times 10^{44} \text{ erg} \times \text{s}^{-1}$ and a global temperature $T_X = 5.61_{-0.71}^{+0.93} \text{ keV}$, where the error bars correspond to the 90% confidence interval. Our measurements are consistent with our results from *Chandra* described above to within 2σ .

Based on the richness- T_X scaling relationship presented by [Rozo & Rykoff \(2014\)](#), we derive a value of ~ 5 keV for T_X for the Champagne Cluster, with a scatter of up to 40%, based on its richness. The values we derive using both *Chandra* and XMM-*Newton* are consistent with this estimate.

5. SPECTROSCOPIC DATA ANALYSIS

Data acquisition: We observed the Champagne Cluster with the DEIMOS multi-object spectrograph ([Faber et al. 2003](#)) at the W. M. Keck Observatory on 2022 July

1 (UT). Because the DEIMOS field of view is approximately $16' \times 4'$, it is ideally suited for observing merging clusters, particularly when the mask’s long axis is placed parallel to the merger axis. We used two slitmasks with a total of 150 (80 and 70, respectively) $1''$ wide slits. We selected potential member galaxies based on Pan-STARRS photometric redshifts ([Beck et al. 2021](#)). Each galaxy in the Pan-Starrs photometric redshift catalog has a redshift uncertainty of σ_{PS} . The likelihood of a given galaxy to be at a cluster at redshift z_{cl} is given by

$$\ell \propto \frac{1}{\sigma_{\text{PS}}} \exp\left(-\frac{(z_{\text{PS}} - z_{\text{cl}})^2}{2\sigma_{\text{PS}}^2}\right)$$

The typical photometric redshift uncertainty of 0.16 enables some focus on the target cluster while also probing foreground and background structures. Additional priority was given to brighter targets.

We used the 1200 line mm^{-1} grating, which results in a pixel scale of $0.33 \text{ \AA pixel}^{-1}$ and a resolution of $\sim 1\text{ \AA}$ (50 km/s). The grating was tilted to observe the wavelength range $\approx 4200\text{--}6900 \text{ \AA}$ (the precise range depends on the slit position), which at $z=0.308$ includes spectral features from the [OII] 3727 \AA doublet to the magnesium line at 5177 \AA . The total exposure time for each mask was 27 minutes divided into three exposures.

Data reduction and redshift extraction: We used PyeIt ([Prochaska et al. 2020](#)) to calibrate the data and reduce it to a series of 1D spectra. We developed a Python software (Pyze) to extract redshifts from 1D spectra. Pyze adopts the approach of the DEEP2 survey ([Newman et al. 2013](#)), which removes a slowly varying empirical continuum model before performing real-space cross-correlation with templates.

This software is described in more detail in [Wittman et al. \(2023\)](#). Since that paper, we have reduced user-to-user redshift variations to the 10^{-5} level by making the redshift refinement more independent of the initial search parameters. The uncertainty is now calculated purely from the curvature of the χ^2 surface, typically yielding uncertainties of $\leq 10^{-4}$ in redshift or ≤ 23 km/s in the frame of the cluster. This does not capture uncertainties in wavelength calibration. These are difficult to quantify, but repeat observations suggest they are at the 10^{-5} level. Table 2 lists the redshifts we obtained through the Keck/DEIMOS run.

¹ https://xmm-tools.cosmos.esa.int/external/xmm_calibration/background/bs_repository/blanksky_all.html

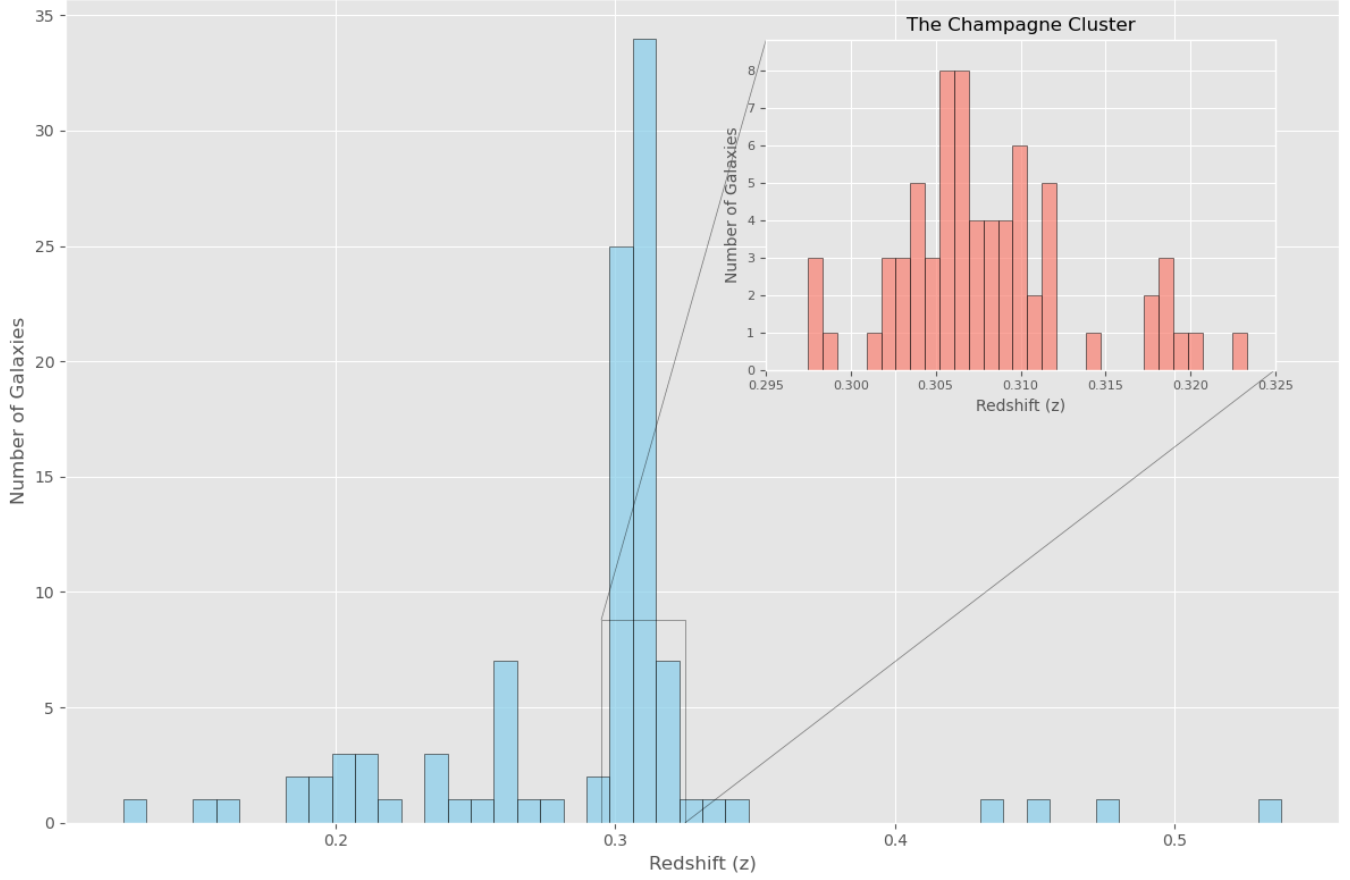


Figure 3. Members of the spectroscopic redshift catalog, with inset showing redshift distribution of potential cluster member galaxies for the Champagne Cluster.

Table 2. Observed redshifts

R.A. (deg)	Decl. (deg)	z	Uncertainty in z
196.406071	26.507350	0.306413	0.000096
196.407129	26.478233	0.307814	0.000078
196.412379	26.482011	0.309665	0.000040
196.413208	26.522172	0.305237	0.000040
196.418250	26.482703	0.307438	0.000040
196.419308	26.490708	0.303361	0.000138
196.420488	26.498347	0.305826	0.000020
196.422767	26.470219	0.320555	0.000049
196.426300	26.484389	0.306604	0.000049
196.430721	26.501328	0.311833	0.000045
196.434650	26.536753	0.310499	0.000035
196.442446	26.515369	0.306663	0.000081
196.447192	26.487183	0.276126	0.000015
196.453525	26.481178	0.302410	0.000048
196.457129	26.487908	0.124041	0.000018

Table 2 *continued*

Table 2 (*continued*)

R.A. (deg)	Decl. (deg)	z	Uncertainty in z
196.460138	26.475936	0.310589	0.000016
196.461229	26.537186	0.307213	0.000023
196.461463	26.509986	0.306062	0.000079
196.466996	26.535747	0.318054	0.000039
196.467113	26.531742	0.197890	0.000004
196.468504	26.512839	0.304628	0.000077
196.473296	26.530936	0.319471	0.000022
196.478412	26.501717	0.310132	0.000075
196.489467	26.509808	0.306763	0.000046
196.495425	26.513433	0.308097	0.000027
196.496883	26.504150	0.340836	0.000039
196.498125	26.515661	0.311543	0.000079
196.500612	26.517731	0.310182	0.000096
196.502837	26.520478	0.306873	0.000097
196.506196	26.529386	0.236583	0.000228

Table 2 *continued*

Table 2 (*continued*)

R.A. (deg)	Decl. (deg)	z	Uncertainty in z
196.511362	26.516389	0.304895	0.000029
196.516858	26.521828	0.318504	0.000141
196.519875	26.551706	0.207438	0.000141
196.521813	26.519706	0.311466	0.000120
196.522946	26.529539	0.314285	0.000041
196.524037	26.531869	0.309698	0.000032
196.533392	26.539300	0.538167	0.000065
196.535112	26.519197	0.297473	0.000056
196.549442	26.566467	0.155595	0.000010
196.549825	26.574411	0.305962	0.000045
196.557217	26.537475	0.306629	0.000106
196.558154	26.525625	0.301910	0.000059
196.560404	26.597644	0.301960	0.000068
196.563408	26.582533	0.236666	0.000073
196.569979	26.576467	0.451659	0.000122
196.574483	26.610456	0.257530	0.000079
196.575971	26.555606	0.303461	0.000014
196.606979	26.547783	0.203394	0.000155
196.609442	26.585897	0.205228	0.000084
196.612413	26.556906	0.473916	0.000033
196.622983	26.623392	0.185849	0.000025
196.633163	26.560635	0.307513	0.000020
196.651542	26.574550	0.158923	0.000377
196.668166	26.584667	0.267854	0.000034
196.671800	26.602144	0.318411	0.000014
196.327725	26.461019	0.305962	0.000234
196.336867	26.436628	0.303811	0.000033
196.340367	26.468936	0.437909	0.000101
196.347869	26.435729	0.256980	0.000024
196.354983	26.437925	0.305562	0.000096
196.355500	26.483536	0.308447	0.000165
196.357233	26.511017	0.304311	0.000014
196.369908	26.466914	0.255032	0.000029
196.373521	26.471492	0.213884	0.001472
196.377208	26.503956	0.306413	0.000048
196.377800	26.468908	0.258414	0.000034
196.380112	26.469231	0.220285	0.000012
196.386390	26.495669	0.303828	0.000037
196.404483	26.496414	0.303311	0.000122
196.410899	26.494889	0.184248	0.000025
196.413475	26.468006	0.303721	0.000061

Table 2 *continued***Table 2** (*continued*)

R.A. (deg)	Decl. (deg)	z	Uncertainty in z
196.419221	26.511228	0.308841	0.000028
196.424454	26.460528	0.309298	0.000072
196.424792	26.513903	0.307623	0.000059
196.439867	26.509047	0.303974	0.000038
196.441833	26.514008	0.309431	0.000042
196.457700	26.510725	0.318771	0.000082
196.462067	26.492536	0.306313	0.000031
196.474878	26.502687	0.297723	0.000118
196.477000	26.502178	0.309465	0.000085
196.480583	26.533928	0.256971	0.000016
196.482008	26.524608	0.307964	0.000247
196.482921	26.508169	0.317520	0.000050
196.484062	26.512369	0.323307	0.000078
196.485979	26.514753	0.305912	0.000029
196.499188	26.565442	0.244575	0.000020
196.502396	26.514214	0.311783	0.000049
196.505046	26.515486	0.309932	0.000104
196.509163	26.569164	0.207280	0.000057
196.514287	26.522178	0.197854	0.000039
196.515092	26.525225	0.199591	0.000008
196.516858	26.541944	0.298207	0.000049
196.530100	26.590400	0.298491	0.000061
196.530583	26.594114	0.337267	0.000046
196.535115	26.548232	0.301142	0.000098
196.536404	26.515406	0.311966	0.000067
196.542904	26.554075	0.304628	0.000121
196.545617	26.582072	0.258731	0.000017
196.556692	26.544931	0.310048	0.000041
196.561896	26.572611	0.258257	0.000046
196.562369	26.572497	0.258254	0.000103
196.568742	26.576467	0.305429	0.000115
196.598842	26.555558	0.237650	0.000034

Archival redshifts acquisition: We found 22 spectroscopic redshifts in NED for galaxies within 10' from the position of the most likely BCG candidate of the Champagne Cluster. We obtained two additional unique redshifts from the Early Data Release of the Dark Energy Spectroscopic Instrument ([DESI Collaboration et al. 2023](#)). This gave us a total of 24 unique archival redshifts. After contrasting the list of 24 unique archival redshift against our Keck/DEIMOS catalog, we found one duplicate. The redshift and velocity differ-

ence between the duplicate archival redshift and the corresponding entry in our Keck/DEIMOS catalog is 3.95×10^{-5} and 12.8 km/s, respectively. After removing the duplicate redshift, we added the remaining 23 redshifts to the 103 redshifts from our Keck/DEIMOS spectroscopic survey to form a final catalog of 126 unique redshifts, which we use in the analysis we undertake in §6.

6. SUBCLUSTERING AND KINEMATICS

We present the members of the spectroscopic redshift catalog in Figure 3. The histogram indicates the presence of a foreground peak of galaxies at $z = 0.260$. This group has a mean redshift of 0.2575 ± 0.0004 and a rest-frame velocity dispersion of 361 ± 96 km/s. Figure 4 shows the locations of all the galaxies in the spectroscopic catalog. We do not see a spatial concentration of the points at $z=0.26$, so we conclude it is not a foreground cluster that would complicate our analysis.

To analyze the dynamics of the Champagne Cluster, we restricted the redshift range to a small window ($0.295 \leq z \leq 0.325$) centered on the redshifts of the cluster’s top BCG candidate (a total of 75 galaxies). We used the biweight estimator (Beers et al. 1990) to calculate the systemic redshift for the Champagne Cluster (0.3069 ± 0.0005) and the velocity dispersion in the cluster rest-frame (1204 ± 155 km/s). We conducted the Anderson-Darling test on the redshift population of the Champagne Cluster to evaluate its consistency with a Gaussian distribution. The resulting p-value of 0.15 indicates that the redshift population of the Champagne Cluster does not deviate significantly from Gaussianity.

We defined Champagne-SE and Champagne-NW as the two clusterings of galaxies appearing, respectively, to the southeast and northwest of the X-ray surface brightness peak as indicated by the dashed-red line in Figure 1. Champagne-SE (Champagne-NW) has 27 (48) spectroscopic galaxy redshifts. We used the biweight method to obtain a systemic redshift for Champagne-SE (Champagne-NW) of 0.3065 ± 0.0012 (0.3069 ± 0.0005) and a velocity dispersion of 1357 ± 171 km/s (1015 ± 242 km/s). Figure 5 illustrates the redshift population of each subcluster. We performed the Anderson-Darling test on the redshift population of each subcluster. The p-value for Champagne-SE is 0.73, indicating that the redshift population fits a single Gaussian distribution well. Champagne-NW has a p-value of 5.15×10^{-5} , suggesting that it significantly deviates from Gaussianity.

We used the average redshift of each subcluster as a proxy for the redshift of the subcluster as a whole to refine the value of the velocity of one cluster in the frame

of the other, Δv_{los} . We get a value of 411 ± 180 km/s. This value is larger than the value we obtained in §2, using the BCGs alone. This value is consistent with the value derived from the BCGs alone at the 2.3σ level, albeit with large uncertainties due to the large velocity dispersion of the member galaxies. It is possible that the BCGs are better tracers of the central part of the potential, but it is difficult to estimate the uncertainty in the relative velocity of the BCGs alone. Therefore, in the modeling that follows we use the result from all member galaxies to avoid overconfidence in the modeling.

Simulated analogs: We searched for analogs to the Champagne Cluster in the Big Multidark Planck Simulation (BigMDPL) (Klypin et al. 2016) using the method of Wittman et al. (2018) and Wittman (2019) with one improvement as follows. Wittman (2019) noted that the velocities listed in the halo catalog are often underestimated when the halos are largely overlapping, resulting in the pericenter speed being biased low. Therefore, they estimate the pericenter speed as the maximum relative halo speed over all snapshots near pericenter. However, we found that this is still biased low compared to the speed that can be inferred from the recorded positions and times. We now infer the speed from the positions and times, which boosts the pericenter speed estimate by 200-400 km/s compared to the old method.

We used the line-of-sight relative velocity (Δv_{21}) that we calculated in §6, and we used the separation between the top two BCG candidates from §2 as a proxy for the separation between the two subclusters. BCGs usually reside near the bottom of the gravitational well, but it is difficult to quantify how near so we assume a generous 100 kpc uncertainty.

In Table 3, we list the 68% confidence interval for the time since pericenter (TSP), pericenter speed v_{max} , viewing angle θ (defined as the angle the subcluster separation vector makes with the line of sight), and φ (defined as the angle the current separation vector makes with the velocity vector). Qualitatively, the relatively low line-of-sight velocity, Δv_{21} , suggests two possibilities: a merger happening near the plane of the sky and/or a merger at turnaround. The combined values of v_{max} and θ (Table 3) seem to prefer a merger near the plane of the sky.

To constrain the scenario further, we used the hydrodynamic, binary merger simulations from the Galaxy Cluster Merger Catalog (<http://gcmc.hub.yt>) (ZuHone 2011). We used different scenarios with different combinations of mass ratios (1:1, 1:3, and 1:10), and impact parameters (0 kpc, 500 kpc, and 1,000 kpc). We compared the peak X-ray emissivity and subcluster location to our data. In the scenario with mass ratio of 1:10

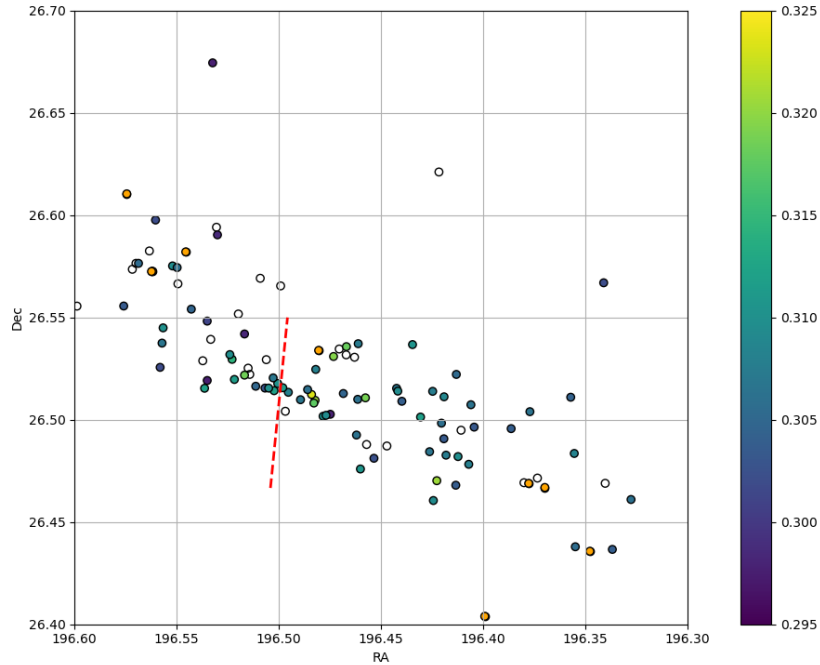


Figure 4. Redshift distribution for the members of the spectroscopic catalog: The Champagne Cluster (color bar), galaxies in the redshift range $0.250 \leq z \leq 0.270$ (orange), and the remaining galaxies (open circles). The dashed line separates the two subclusters, Champagne-NW and Champagne-SE.

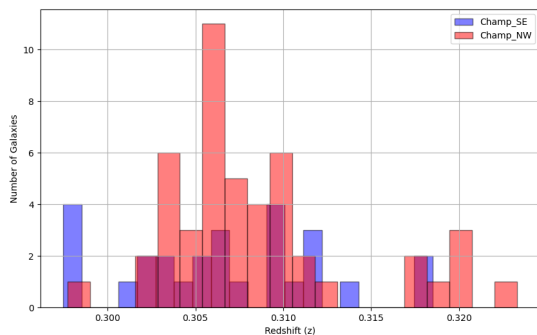


Figure 5. The two subclusters of the Champagne Cluster: Champagne-SE and Champagne-NW.

and impact parameter of 0 kpc in an inbound post first-pericenter phase, the location of the peak X-ray surface brightness between the two mass density peaks resembles the scenario we have. The simulations with the 500 and 1000 kpc impact parameters did not resemble the Champagne cluster, strengthening the case for a small impact parameter.

7. CONCLUSIONS

Table 3. Dynamical parameters from analogs

TSP (Myr)	v_{\max} (km/s)	θ (deg)	φ (deg)
68% CI			
85–271	1589–2205	55–85	7–35
95% CI			
20–381	1371–2631	30–89	2–120

We have presented a new bimodal galaxy cluster merger, the Champagne Cluster, with a number of remarkable features. The offset between the X-ray peak and the BCGs of the subclusters suggests that the collision trajectory was near head-on. The low line of sight velocity difference between the two subclusters involved in the merger (Champagne-SE and Champagne-NW), in addition to simulated analogs, indicate the merger is happening mainly in the plane of the sky. These features make the Champagne Cluster a promising system for follow-up as it can potentially shed some more light on the reaction of dark matter to a high speed collision. High-resolution weak lensing and X-ray maps could constrain the dynamics further by providing accurate estimates for the masses of the subclusters, as well as offsets between the mass centroids and the X-ray emission peak

and the presence of shocks and temperature or density discontinuities.

8. ACKNOWLEDGEMENTS

This work was supported by NSF grant 2308383.

This research has made use of data obtained from the *Chandra* Data Archive and the *Chandra* Source Catalog, and of *Aladin sky atlas* developed at CDS, Strasbourg Observatory, France (Bonnarel et al. 2000). It has also made use of software provided by the *Chandra* X-ray Center (CXC) in the application packages CIAO-4.14 (Fruscione et al. 2006) and Sherpa (Freeman et al. 2001).

This research has also made use of data data obtained from the Legacy Surveys. The Legacy Surveys consist of three individual and complementary projects: the Dark Energy Camera Legacy Survey (DECaLS; Proposal ID :2014B-0404; PIs: David Schlegel and Arjun Dey), the Beijing-Arizona Sky Survey (BASS; NOAO Prop. ID:015A-0801; PIs: Zhou Xu and Xiaohui Fan), and the Mayall z-band Legacy Survey (MzLS; Prop. ID :2016A-0453; PI: Arjun Dey). DECaLS, BASS and MzLS together include data obtained, respectively, at the Blanco telescope, Cerro Tololo Inter-American Observatory, NSF’s NOIRLab; the Bok telescope, Steward Observatory, University of Arizona; and the Mayall telescope, Kitt Peak National Observatory, NOIRLab. Pipeline processing and analyses of the data were supported by NOIRLab and the Lawrence Berkeley National Laboratory (LBNL). The Legacy Surveys project is honored to be permitted to conduct astronomical research on Iolkam Du’ag (Kitt Peak), a mountain with particular significance to the Tohono O’odham Nation.

NOIRLab is operated by the Association of Universities for Research in Astronomy (AURA) under a cooperative agreement with the National Science Foundation. LBNL is managed by the Regents of the University of California under contract to the U.S. Department of Energy.

This project used data obtained with the Dark Energy Camera (DECam), which was constructed by the Dark Energy Survey (DES) collaboration. Funding for the DES Projects has been provided by the U.S. Department of Energy, the U.S. National Science Foundation, the Ministry of Science and Education of Spain, the Science and Technology Facilities Council of the United Kingdom, the Higher Education Funding Council for England, the National Center for Supercomput-

ing Applications at the University of Illinois at Urbana-Champaign, the Kavli Institute of Cosmological Physics at the University of Chicago, Center for Cosmology and Astro-Particle Physics at the Ohio State University, the Mitchell Institute for Fundamental Physics and Astronomy at Texas A&M University, Financiadora de Estudos e Projetos, Fundacao Carlos Chagas Filho de Amparo, Financiadora de Estudos e Projetos, Fundacao Carlos Chagas Filho de Amparo a Pesquisa do Estado do Rio de Janeiro, Conselho Nacional de Desenvolvimento Cientifico e Tecnologico and the Ministerio da Ciencia, Tecnologia e Inovacao, the Deutsche Forschungsgemeinschaft and the Collaborating Institutions in the Dark Energy Survey. The Collaborating Institutions are Argonne National Laboratory, the University of California at Santa Cruz, the University of Cambridge, Centro de Investigaciones Energeticas, Medioambientales y Tecnologicas-Madrid, the University of Chicago, University College London, the DES-Brazil Consortium, the University of Edinburgh, the Eidgenossische Technische Hochschule (ETH) Zurich, Fermi National Accelerator Laboratory, the University of Illinois at Urbana-Champaign, the Institut de Ciencies de l’Espai (IEEC/CSIC), the Institut de Fisica d’Altes Energies, Lawrence Berkeley National Laboratory, the Ludwig Maximilians Universitat Munchen and the associated Excellence Cluster Universe, the University of Michigan, NSF’s NOIRLab, the University of Nottingham, the Ohio State University, the University of Pennsylvania, the University of Portsmouth, SLAC National Accelerator Laboratory, Stanford University, the University of Sussex, and Texas A&M University.

BASS is a key project of the Telescope Access Program (TAP), which has been funded by the National Astronomical Observatories of China, the Chinese Academy of Sciences (the Strategic Priority Research Program “The Emergence of Cosmological Structures” Grant # XDB09000000), and the Special Fund for Astronomy from the Ministry of Finance. The BASS is also supported by the External Cooperation Program of Chinese Academy of Sciences (Grant # 114A11KYSB20160057), and Chinese National Natural Science Foundation (Grant # 12120101003, # 11433005).

Facilities: Keck:II (Deimos), Chandra, XMM.

This work made use of data from the Galaxy Cluster Merger Catalog (<http://gcmc.hub.yt>)

REFERENCES

- Aihara, H., Allende Prieto, C., An, D., et al. 2011, ApJS, 193, 29, doi: [10.1088/0067-0049/193/2/29](https://doi.org/10.1088/0067-0049/193/2/29)
- Arnaud, K. A. 1996, in Astronomical Society of the Pacific Conference Series, Vol. 101, Astronomical Data Analysis Software and Systems V, ed. G. H. Jacoby & J. Barnes, 17

- Arnaud, M., Majerowicz, S., Lumb, D., et al. 2002, *A&A*, 390, 27, doi: [10.1051/0004-6361:20020669](https://doi.org/10.1051/0004-6361:20020669)
- Beck, R., Szapudi, I., Flewelling, H., et al. 2021, *MNRAS*, 500, 1633, doi: [10.1093/mnras/staa2587](https://doi.org/10.1093/mnras/staa2587)
- Beers, T. C., Flynn, K., & Gebhardt, K. 1990, *AJ*, 100, 32, doi: [10.1086/115487](https://doi.org/10.1086/115487)
- Bonnarel, F., Fernique, P., Bienaymé, O., et al. 2000, *A&AS*, 143, 33, doi: [10.1051/aas:2000331](https://doi.org/10.1051/aas:2000331)
- Botteon, A., Shimwell, T. W., Cassano, R., et al. 2022, *A&A*, 660, A78, doi: [10.1051/0004-6361/202143020](https://doi.org/10.1051/0004-6361/202143020)
- Bradač, M., Allen, S. W., Treu, T., et al. 2008, *ApJ*, 687, 959, doi: [10.1086/591246](https://doi.org/10.1086/591246)
- Carter, J. A., & Read, A. M. 2007, *A&A*, 464, 1155, doi: [10.1051/0004-6361:20065882](https://doi.org/10.1051/0004-6361:20065882)
- Clowe, D., Bradač, M., Gonzalez, A. H., et al. 2006, *ApJL*, 648, L109, doi: [10.1086/508162](https://doi.org/10.1086/508162)
- Cohn, J., & White, M. 2005, *Astroparticle Physics*, 24, 316, doi: <https://doi.org/10.1016/j.astropartphys.2005.07.006>
- Dawson, W. A., Wittman, D., Jee, M., et al. 2011, *ArXiv e-prints*. <https://arxiv.org/abs/1110.4391>
- DESI Collaboration, Adame, A. G., Aguilar, J., et al. 2023, *arXiv e-prints*, arXiv:2306.06308, doi: [10.48550/arXiv.2306.06308](https://doi.org/10.48550/arXiv.2306.06308)
- Faber, S. M., Phillips, A. C., Kibrick, R. I., et al. 2003, in *Society of Photo-Optical Instrumentation Engineers (SPIE) Conference Series*, Vol. 4841, *Instrument Design and Performance for Optical/Infrared Ground-based Telescopes*, ed. M. Iye & A. F. M. Moorwood, 1657–1669, doi: [10.1117/12.460346](https://doi.org/10.1117/12.460346)
- Freeman, P., Doe, S., & Siemiginowska, A. 2001, in *Society of Photo-Optical Instrumentation Engineers (SPIE) Conference Series*, Vol. 4477, *Astronomical Data Analysis*, ed. J.-L. Starck & F. D. Murtagh, 76–87, doi: [10.1117/12.447161](https://doi.org/10.1117/12.447161)
- Frank, C. S., & White, S. D. M. 2012, *Annalen der Physik*, 524, 507, doi: [10.1002/andp.201200212](https://doi.org/10.1002/andp.201200212)
- Fruscione, A., McDowell, J. C., Allen, G. E., et al. 2006, in *Society of Photo-Optical Instrumentation Engineers (SPIE) Conference Series*, Vol. 6270, *Society of Photo-Optical Instrumentation Engineers (SPIE) Conference Series*, ed. D. R. Silva & R. E. Doxsey, 62701V, doi: [10.1117/12.671760](https://doi.org/10.1117/12.671760)
- Klypin, A., Yepes, G., Gottlöber, S., Prada, F., & Heß, S. 2016, *MNRAS*, 457, 4340, doi: [10.1093/mnras/stw248](https://doi.org/10.1093/mnras/stw248)
- Kravtsov, A. V., & Borgani, S. 2012, *Annual Review of Astronomy and Astrophysics*, 50, 353, doi: [10.1146/annurev-astro-081811-125502](https://doi.org/10.1146/annurev-astro-081811-125502)
- Mahdavi, A., Hoekstra, H., Babul, A., Balam, D. D., & Capak, P. L. 2007, *The Astrophysical Journal*, 668, 806–814, doi: [10.1086/521383](https://doi.org/10.1086/521383)
- Mansheim, A. S., Lemaux, B. C., Tomczak, A. R., et al. 2017, *Monthly Notices of the Royal Astronomical Society: Letters*, 469, L20, doi: [10.1093/mnrasl/slx041](https://doi.org/10.1093/mnrasl/slx041)
- Markevitch, M., Gonzalez, A. H., Clowe, D., et al. 2004, *ApJ*, 606, 819, doi: [10.1086/383178](https://doi.org/10.1086/383178)
- Miller, N. A., & Owen, F. N. 2003, *AJ*, 125, 2427, doi: [10.1086/374767](https://doi.org/10.1086/374767)
- Newman, J. A., Cooper, M. C., Davis, M., et al. 2013, *ApJS*, 208, 5, doi: [10.1088/0067-0049/208/1/5](https://doi.org/10.1088/0067-0049/208/1/5)
- Okabe, N., & Umetsu, K. 2008, *PASJ*, 60, 345, doi: [10.1093/pasj/60.2.345](https://doi.org/10.1093/pasj/60.2.345)
- Prochaska, J. X., Hennawi, J., Cooke, R., et al. 2020, *pypeit/PypeIt: Release 1.0.0, v1.0.0*, Zenodo, Zenodo, doi: [10.5281/zenodo.3743493](https://doi.org/10.5281/zenodo.3743493)
- Randall, S. W., Markevitch, M., Clowe, D., Gonzalez, A. H., & Bradač, M. 2008, *ApJ*, 679, 1173, doi: [10.1086/587859](https://doi.org/10.1086/587859)
- Rozo, E., & Rykoff, E. S. 2014, *The Astrophysical Journal*, 783, 80, doi: [10.1088/0004-637X/783/2/80](https://doi.org/10.1088/0004-637X/783/2/80)
- Rykoff, E. S., Rozo, E., Busha, M. T., et al. 2014, *ApJ*, 785, 104, doi: [10.1088/0004-637X/785/2/104](https://doi.org/10.1088/0004-637X/785/2/104)
- Rykoff, E. S., Rozo, E., Hollowood, D., et al. 2016, *The Astrophysical Journal Supplement Series*, 224, 1, doi: [10.3847/0067-0049/224/1/1](https://doi.org/10.3847/0067-0049/224/1/1)
- Simet, M., McClintock, T., Mandelbaum, R., et al. 2016, *Monthly Notices of the Royal Astronomical Society*, 466, 3103, doi: [10.1093/mnras/stw3250](https://doi.org/10.1093/mnras/stw3250)
- Stancioli, R., Wittman, D., Finner, K., & Bouhrik, F. 2024, *ApJ*, 966, 49, doi: [10.3847/1538-4357/ad3249](https://doi.org/10.3847/1538-4357/ad3249)
- Wittman, D. 2019, *The Astrophysical Journal*, 881, 121, doi: [10.3847/1538-4357/ab3052](https://doi.org/10.3847/1538-4357/ab3052)
- Wittman, D., Golovich, N., & Dawson, W. A. 2018, *ApJ*, 869, 104, doi: [10.3847/1538-4357/aaee77](https://doi.org/10.3847/1538-4357/aaee77)
- Wittman, D., Stancioli, R., Finner, K., et al. 2023, *The Astrophysical Journal*, 954, 36, doi: [10.3847/1538-4357/acdb73](https://doi.org/10.3847/1538-4357/acdb73)
- Wright, E. L. 2006, *PASP*, 118, 1711, doi: [10.1086/510102](https://doi.org/10.1086/510102)
- ZuHone, J. A. 2011, *ApJ*, 728, 54, doi: [10.1088/0004-637X/728/1/54](https://doi.org/10.1088/0004-637X/728/1/54)